IEEE Robotics and Automation Letters (RAL) paper presented at
2024 IEEE/RSJ International Conference on Intelligent Robots and Systems (IROS)
October 14-18, 2024. Abu Dhabi, UAE

Transformable Nano Rover for Space Exploration

Daichi Hirano, Mariko Inazawa, Masataku Sutoh, Hirotaka Sawada, Yuta Kawai, Masaharu Nagata, Gen Sakoda, Yousuke Yoneda, and Kimitaka Watanabe

***Abstract*—This letter introduces a novel nano rover designed to transform its shape for efficient movement on lunar surfaces. The rover, resembling a compact ball, has a diameter of roughly 80 mm and a mass around 250 g. Its transformational mechanism allows for compactness during planetary transportation, with enhanced mobility achieved through the use of extendable wheels, a tail stabilizer, and cameras. To traverse soft terrains efficiently, the rover utilizes an eccentric wheel mechanism, offering two distinct movement modes based on wheel synchronization. This mechanism provides a locomotion velocity of 20 mm/s or more on a flat surface. Moreover, it features onboard image processing to detect spacecraft shielded by Multi-Layer Insulation (MLI) films, facilitating autonomous control and selective image transmission. This rover has been deployed in a real space mission, having been mounted on a lunar lander. This letter presents the design specifics of this transformable rover and results from field tests simulating lunar conditions. These tests affirmed the efficacy of the proposed motion mechanism and onboard image processing.**

***Index Terms*—Space robotics and automation, wheeled robots, micro/nano robots, computer vision for automation, vision-based navigation.**

I. Introduction

ROBOTICS played a pivotal role in advancing space exploration, particularly collecting vital data from planets and asteroids. Notable instances in lunar exploration include the remotely operated Lunokhods 1 and 2, which were deployed on the Moon for the first time in the 1970s [1]. Additionally, the lunar rovers Yutu and Yutu-2 recently traveled the lunar surface in 2013 and 2019, respectively [2]. Furthermore, the Pragyan rover made history in 2023 by exploring the Moon's South Pole region for the first time. Looking ahead, the VIPER and LUPEX rovers, weighing 430 and 350 kg, respectively, will be launched in the mid-2020 s to explore the water resources of the Moon [3], [4]. These large rovers have long activity times and high locomotion capabilities to transverse stably on rough terrains and carry a variety of scientific instruments. Micro/nano rovers, characterized by their compactness, lightweight, and cost-effectiveness, have gained prominence in space exploration. Despite limitations in mission time and payload capacity, these rovers offer independent operation through wireless connections, performing tasks such as collecting soil samples and capturing unique images from angles inaccessible to a larger primary spacecraft. Over the past few years, there has been a growing demand for such intelligent small rovers in challenging missions.

Addressing the demand for cost-effective robotic capabilities, the Japan Aerospace Exploration Agency (JAXA) has developed a palm-sized wheeled rover tailored for capturing images and collecting scientific data for lunar exploration. This rover is designed to move around a primary spacecraft, capturing imagery data and transmitting it wirelessly. Featuring two cameras and an onboard computer that executes image analysis, it can detect multi-layer insulation (MLI) films for finding a primary spacecraft. The rover can be folded into a compact ball shape (approximately 80 mm diameter and 250 g mass) for storage on a spacecraft, incorporating deployable hemispherical wheels, a tail stabilizer, and cameras for transversing rough terrains, as illustrated in Fig. 1. Its lightweight and compact form facilitates its integration into a primary lander, thus utilizing minimal payload mass and space. To our current understanding, this

Fig. 1. Picture of the transformable nano rover. The ball-shaped rover on the left side transforms to the wheeled rover on the right side.

Manuscript received 11 September 2023; accepted 14 January 2024. Date of publication 7 February 2024; date of current version 22 February 2024. This letter was recommended for publication by Associate Editor M. Russo and Editor C. Gosselin upon evaluation of the reviewers' comments. *(Corresponding author: Daichi Hirano.)*

Daichi Hirano and Mariko Inazawa are with Research and Development Directorate, Japan Aerospace Exploration Agency, Tsukuba 305-8505, Japan (e-mail: hirano.daichi@jaxa.jp; inazawa.mariko@jaxa.jp).

Masataku Sutoh and Hirotaka Sawada are with Space Exploration Innovation Hub Center, Japan Aerospace Exploration Agency, Sagamihara 252-5210, Japan (e-mail: sutoh.masataku@jaxa.jp; sawada.hirotaka@jaxa.jp).

Yuta Kawai is with Human Spaceflight Technology Directorate, Japan Aerospace Exploration Agency, Tsukuba 305-8505, Japan (e-mail: kawai.yuta@jaxa.jp).

Masaharu Nagata and Gen Sakoda are with Exploratory Deployment Group, Sony Group Corporation, Tokyo 141-8610, Japan (e-mail: masaharu.nagata@sony.com; gen.sakoda@sony.com).

Yousuke Yoneda is with Technology Development Division, TOMY Company Ltd., Tokyo 125-8503, Japan (e-mail: y.yoneda@takaratomy.co.jp).

Kimitaka Watanabe is with the Faculty of Life and Mecdical Sciences, Doshisha University, Kyoto 610-0394, Japan (e-mail: kiwatana@mail.doshisha.ac.jp).

This letter has supplementary downloadable material available at https://doi.org/10.1109/LRA.2024.3363529, provided by the authors.

Digital Object Identifier 10.1109/LRA.2024.3363529

2377-3766 © 2024 IEEE. Personal use is permitted, but republication/redistribution requires IEEE permission.
See https://www.ieee.org/publications/rights/index.html for more information.

Copyright ©2024 IEEE

Authorized licensed use limited to: Japan Aerospace Exploration Agency. Downloaded on February 27,2024 at 09:27:31 UTC from IEEE Xplore. Restrictions apply.

TABLE I
MICRO/NANO ROVER COMPARISON

Rover	Target site	Mass	Deployed size	Locomotion unit	Velocity	Power resources
Prop-M*	Mars	4.5 kg	215×160×60 mm	2 skis	0.28 mm/s	Wired supply from a lander
Sojourner*	Mars	11.5 kg	650×480×300 mm	6 wheels (dia. 130 mm)	10 mm/s	Solar array & non-rechargeable battery
Nanorover [7]	Asteroid	1.3 kg	140×140×60 mm	4 wheels (dia. 65 mm)	1.5 mm/s	Solar cells (no battery)
Nanokhod [8]	Mars	1.4 kg	240×165×65 mm	2 crawlers	0.83 mm/s	Wired supply from a lander
Micro5 [9]	The Moon	5 kg	550×530×250 mm	5 wheels (dia. 100 mm)	15 mm/s	Solar panel & battery
LEV-2 (Ours)*	The Moon	0.25 kg	123×136×90 mm	2 wheels (dia. 78 mm)	20 mm/s	Non-rechargeable battery

*These rovers were launched. Others are cancelled or under development.

rover ranks as the smallest lunar rover ever launched. Moreover, the deployment of wheels and stabilizer significantly improves the rover's mobility and stability during surface exploration. Additionally, the design incorporates eccentric rotation wheels for specific movements on softer terrains.

Flight models of this rover were crafted for two distinct space missions. The first was the HAKUTO-R Mission 1 [5]. In this mission, the rover was incorporated into a lander and was successfully launched into lunar orbit. Unfortunately, this mission did not achieve a soft lunar landing. The subsequent mission is JAXA's Smart Lander for Investigating Moon (SLIM), which was successfully launched in September 2023 [6]. Within the SLIM mission, this rover is named the Lunar Excursion Vehicle 2 (LEV-2) and is autonomously directed to move and photograph the vicinity of the SLIM lander. For these space missions, we conducted space environment tests encompassing vibration and thermal vacuum evaluations. These tests affirmed the rovers' preparedness to withstand the challenges of launch and lunar landing.

This research delineates the design aspects of a transformable nano rover dispatched to the Moon, detailing its motion mechanisms and diverse functionalities, employing an onboard computer, sensors, and a wireless communication apparatus. The letter also outlines practical mission approaches utilizing this rover through various control modes. Conclusively, we showcase experimental outcomes from field tests conducted in simulated lunar conditions.

II. RELATED WORKS

Compared to traditional large exploration rovers, micro/nano rovers offer distinct advantages. Micro/nano rovers, with their ability to be seamlessly integrated onto spacecraft with stringent mass restrictions and at a fraction of the cost, serve as invaluable payloads for high-risk scientific investigations and technological demonstrations. Consequently, a number of compact vehicles have been proposed for planetary exploration and subsequently evaluated in space environment tests. In Table I, we made comparisons among the proposed rover and previously developed micro/nano rovers weighing 10 kg or less and launched similar class rovers. The Soviet Union sent the first Martian rover named Prop-M aboard the Mars 2 and 3 missions, which regrettably failed in 1971. NASA Jet Propulsion Laboratory (JPL) launched Sojourner that became the first successful rover exploring the Martian terrain in 1997. Subsequently, several space agencies developed micro rovers, including Nanorover for JAXA's Hayabusa mission in JPL [7], Nanokhod rover in European Space Agency (ESA) [8], and Micro5 rover in JAXA [9]. In contrast to these rovers, our nano rover has limitations in carrying large payloads and faces restricted mission time due to its compact volume design without solar cells or a power supply cable from a primary lander. Alternatively, the distinguishing feature of our nano rover lies in its ultralight and fast two-wheeled design. It prioritizes essential equipment and high-speed locomotion, enabling it to cover a substantial area in a restricted mission time. This emphasis on mass and locomotion velocity positions the nano rover as a unique and potentially efficient asset for specific exploration scenarios.

In recent years, diverging from the conventional space agency missions, the Commercial Lunar Payload Services (CLPS) initiative has gained traction among numerous universities and private firms, promoting the launch of micro/nano rovers on the Moon. Carnegie Mellon University, for example, has designed the shoebox-sized, 2 kg rover named Iris [10]. TU Delft is constructing a six-legged rover known as Lunar Zebro [11]. Dymon Co., Ltd. has developed a compact two-wheeled vehicle called YAOKI, which has mass of 0.498 kg and size of $150 \times 150 \times 100$ mm [12]. Although the YAOKI rover belongs to the same class of small two-wheeled vehicle, our rover stands out as the lightest and most compact model.

Furthermore, recent discussions have underscored the importance of exploration, wherein small intelligent robots that collaboratively operate within wireless networks to conduct thorough and efficient planetary investigations. NASA's JPL has developed three shoebox-sized rovers to showcase the potential of autonomous multi-agent systems in collaborative exploration [13]. This program is named Cooperative Autonomous Distributed Robotic Exploration (CADRE), which is a follow-on from an origami-inspired Mars rover featuring a collapsible pop-up chassis that could be compacted for storage [14]. Our rover can be applied to such a multi-agent collaborative exploration, but it is not explored in this letter.

III. DESIGN

A. System Architecture Overview

The hardware design of the proposed rover is depicted in Fig. 2. The rover features a primary body, a head, an attitude stabilizer, and hemispherical wheels. When folded, the rover is encased by these hemispherical wheels, which later extend to both sides of the main body post-transformation. The deployed rover size is approximately $123 \times 136 \times 90$ mm, while it is folded in a ball shape with a diameter of roughly 80 mm before

Authorized licensed use limited to: Japan Aerospace Exploration Agency. Downloaded on February 27,2024 at 09:27:31 UTC from IEEE Xplore. Restrictions apply.

Fig. 2. Deployable components on the rover. The head and the tail stabilizer are deployed after the wheels extend.

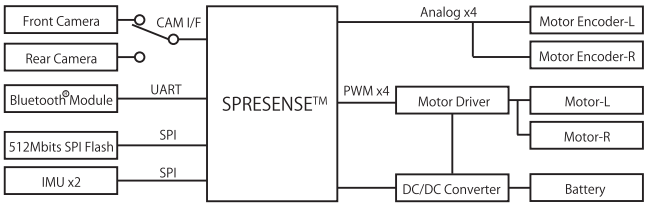

Fig. 3. System architecture of the transformable nano rover. The onboard computer SPRESENSE™ processes all sensors and actuators.

TABLE II
CAMERA DEVICE SPECIFICATIONS

	Specifications	Remarks
Image sensor	1/4″ type CMOS image sensor	Sony ISX012
Resolution	160×120 - 2560×1920 pixels	
ISO sensitivity	ISO 40 - 800	Automatic exposure supported
Shutter speed	1/8 - 1/42000 sec.	
Lens	FOV 100°	Fixed focus

the deployment. The head, designed to rise upwards, houses two onboard cameras located at its front and rear for photography. A Bluetooth module for wireless communication is also housed within the head, thus it is crafted from a space-tolerant material permitting radio wave transmission. The stabilizer, reminiscent of a tail, extends backward, supporting the main body to prevent any backward tilting during forward motion.

B. Electronics

Fig. 3 presents the electrical architecture. The onboard computer is designed to possess both the computational prowess and the varied interfaces essential for autonomous driving control. Furthermore, the onboard computer should be energy-efficient, compact, and lightweight to maintain the rover's streamlined design. To meet these requirements, we used SPRESENSE™ as an onboard computer manufactured by Sony Semiconductor Solutions Corporation. The onboard computer possesses the ability to monitor and control the camera, wheel motors, and wireless communication devices. It also acquires sensor data from the camera, IMUs, and absolute encoders to calculate wheel angles, subsequently storing this data in the SPI flash memory. The camera specifications are summarized in Table II. Moreover, the computer administers the autonomous control sequence and carries out image processing, as elaborated in subsequent sections. Radiation tests were executed on each device, revealing that this onboard computer maintains adequate radiation tolerance

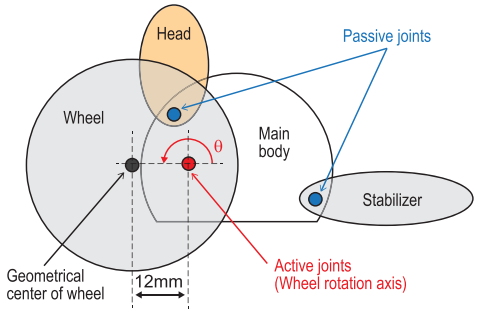

Fig. 4. Schematic diagram of the rover. The wheel is rotated around a point displaced from the geometric center of wheel to increase the reachable distance of the wheel from the main body. The absolute wheel angle θ is measured by the encoders.

for lunar transportation and surface operations by employing a protective shield of 2 mm thick aluminum.

The sole power source is a non-rechargeable battery with a capacity of 6000 mWh. To streamline the system, no solar cells or rechargeable batteries are integrated. Mission time on the Moon depends on the surface temperature because the efficiency of a dc/dc converter connecting with the battery decreases at low temperature. This rover operates for a minimum of 2 h at −20 °C, and it is expected to operate for more than twice that duration during our mission planning operations at approximately 50 °C.

C. Actuators

This rover is driven by only two motors through PWM duty commands from the onboard computer. Each motor connects to a wheel via gear units, allowing independent control and enabling the rover to move forward and turn on surfaces. The rover incorporates brushed dc motors and gearboxes with a gear ratio of 256:1, providing a maximum rotational speed of 270 deg/s and maximum torque of approximately 109 mNm at the wheel axes. The power consumption per motor is approximately 180 mW. Encoders connected to the gear units measure the absolute angle of the wheels. Notably, the same motors serve for deployment and movement functions.

The locomotion units lack elaborate sealing to protect against dusty regolith soil. Instead, the shafts are pressed to sufficiently eliminate mechanical gaps with the main body shield. Furthermore, the rotational shafts and gears are coated with a layer of MoS_2 to reduce friction with dusty regolith soils in case they invade the shielded body. In instances where the gears stop due to dust contamination, prompting the motors to autonomously reverse and unlock the gears.

D. Deployable Mechanism

A schematic diagram of the deployed rover is briefly illustrated in Fig. 4. The rover has two passive joints to deploy the head and the stabilizer. In contrast, the two wheels are driven actively by the motors.

Fig. 5 illustrates the motor-driven rotational shaft (in green), which is equipped with two convex protrusions. Surrounding the shaft axis of the main body housing structure are keyholes

Authorized licensed use limited to: Japan Aerospace Exploration Agency. Downloaded on February 27,2024 at 09:27:31 UTC from IEEE Xplore. Restrictions apply.

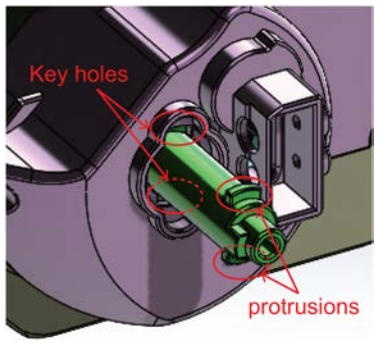

Fig. 5. Wheel shaft is deployed through the key holes along the main body's side shield.

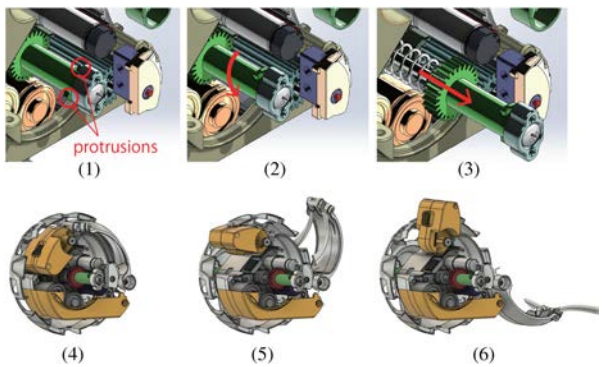

Fig. 6. Transformational mechanism and sequence. The rotational shaft pushes the hemispherical wheels outward to ensure that the head and tail stabilizer are deployed.

that align with the shape of these protrusions. The mechanism within the rover for deployment is depicted in Fig. 6. In the folding configuration described by image (1), the shaft remains constrained within the main body due to the asynchronization between the shaft protrusions and the keyhole shape. By actuating the motor in step (2) to synchronize the shaft protrusions with the keyhole, a mechanical spring in step (3) propels the shaft through the keyhole. This action deploys the wheels with the shafts in step (4). Following this, in step (5), the head and attitude stabilizer are passively deployed by mechanical springs; they are initially concealed and confined by the wheels. Ultimately, all deployable components achieve full expansion in step (6). The transformational process is irreversible, ensuring that the rover maintains its deployed configuration once expanded. This deployable mechanism draws inspiration from transformational technologies employed in commercial toys.

E. Motion Mechanism

The left and right wheels operate synchronously, granting the rover the ability to deploy and move forward on surface. During straight-ahead driving, the wheel angles are synchronized using the absolute encoders. For each rotation, the fast-rotating wheel reaches one rotation ahead and waits for the other slow-rotating wheel to align at the same phase. Additionally, the rover turns by rotating the wheels in directions opposite to each other, but lacks the ability to move backward.

Fig. 7. Motion sequence of the eccentric wheel. This eccentric rotation allows the rover to sweep the wheels with a longer stroke.

Small wheels often face challenges when overcoming slopes and obstacles. To address this issue, the rotation axis was intentionally shifted by 12 mm from the geometric center of a 78 mm diameter wheel, as depicted in Fig. 4. This eccentric rotation results in an increased reachable distance of the wheel from the rotational shaft, as shown in Fig. 7. This design enhancement improves mobility, allowing the rover to navigate over slopes and obstacles more effectively.

The two eccentric wheels operate independently, giving rise to two distinct movement modes contingent upon the angular phases of the wheels. The first mode involves a symmetrical "butterfly" stroke motion wherein both wheels move in tandem. The second mode entails a "crawl" stroke motion where wheel synchronization is absent. During the butterfly motion, the rover's main body maintains a consistent roll attitude due to synchronous wheel rotation. However, when the longer side of the wheels contacts the surface, the main body experiences vertical movement. In contrast, the crawling motion induces angular oscillation in the main body's roll axis while minimizing vertical displacement. The practical impact of eccentric wheel rotation and the performance of these diverse modes were confirmed through a field test discussed in a subsequent section.

Upon landing and transformation on the lunar surface, the rover's orientation is uncertain, which might result in an initial upside-down attitude. Moreover, the rover could encounter situations where it topples over obstacles, leading to an inverted position. To counter such scenarios, the rover utilizes its acceleration output to automatically detect unfavorable orientations and rectify them by propelling the wheels forward to regain an upright stance. Following this corrective motion, the rover effectively maneuvers across the surface.

When the rover encounters large obstacles, such situations cannot be automatically detected by the rover. Therefore, collision avoidance with such obstacles requires manual intervention through remote control. Monitoring is facilitated using onboard images or perspective images captured by a camera mounted on a lander. Alternatively, in an autonomous control scheme, the rover repeats a procedure of moving forward and turning around in a sequential manner until a target lander is found using image processing described in the next section, to leave an obstacle blocked area, or a slope/hill where occludes the direct sight of the lander.

IV. Image Processing

A. Image Processing Overview

The images captured by the head cameras serve a dual purpose: aiding in relative navigation to a parent spacecraft and

Authorized licensed use limited to: Japan Aerospace Exploration Agency. Downloaded on February 27,2024 at 09:27:31 UTC from IEEE Xplore. Restrictions apply.

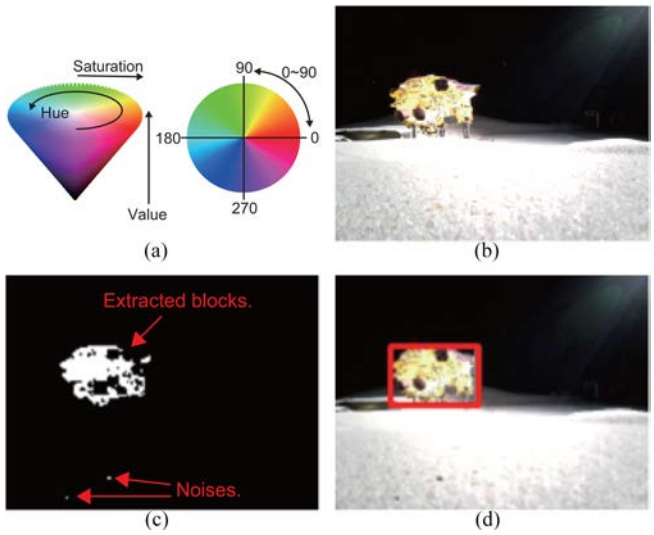

Fig. 8. HSV color space and sample images of the detection algorithm. (a) HSV color chart showing the parameters used in the image processing. (b) Original image. (c) Extracted pixels satisfying $H \leqq 90$ and $S * V \geqq 7000$ and grouping as blocks. (d) Detection result showing a rectangle enclosing remaining blocks after eliminating outliers as noises.

autonomously selecting images for transmission. Spacecraft are typically shielded with MLI blankets to thermally insulate them and maintain temperature. We devised an algorithm for onboard detection of spacecraft covered by MLI blankets, employing limited computational resources. The image processing employs low-resolution images of 160 × 120 pixels directly captured by the camera. In contrast, transmitted images are captured at high resolution, reaching up to 5 megapixels. The compression rate is adjusted to maintain a transferable data size.

B. Detection Algorithm

We photographed MLI films under various exposure conditions in an environment simulating the lunar surface, revealing the following findings. First, the gray-colored lunar surface facilitates the detection of the MLI color. A specific range of Hue (H) can be utilized for detecting the MLI in the HSV color space, as shown in Fig. 8(a). Second, pixels that distinctly capture MLI can be extracted by using Saturation (S) and Value (V).

The flowchart of the detection algorithm is depicted in Fig. 9. Beginning with a low-resolution image, the image's contrast is enhanced through histogram equalization. After converting the image's color space from YUV to HSV, the algorithm identifies regions of MLI blanket coloration in the image. A binary image is generated with detected MLI areas as white and the rest as black. The process involves extracting pixels satisfying two conditions: hues within the constrained range THL_H, similar to MLI's polyimide films, and a value obtained by multiplying saturation and value $S*V$ meeting or exceeding threshold THL_{SV1}. If the maximum $S*V$ value among extracted pixels falls below threshold THL_{SV2}, it indicates the absence of the target spacecraft in the image. In cases of detection, the algorithm identifies blobs in the binarized image, eliminating small ones

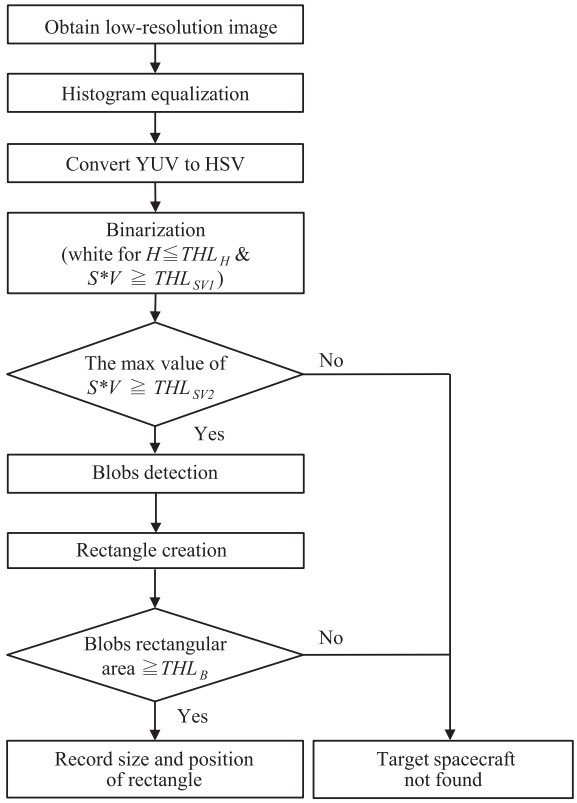

Fig. 9. Flowchart of the detection algorithm. This process is performed onboard.

as noise. A rectangle encompassing all blobs is formed. If the rectangle's area surpasses threshold THL_B, the presence of the target spacecraft is confirmed. Ultimately, the rectangle's sides' lengths and position are documented. Sample images illustrating this process are displayed in Fig. 8.

The length of the identified rectangle enabled estimation of the relative distance to the MLI-covered parent spacecraft. Furthermore, by analyzing the position of the detected rectangle in the image, the relative attitude to the parent spacecraft was calculated. These estimations play a pivotal role in navigating and autonomously controlling movement around the parent spacecraft.

In challenging scenarios where this algorithm may not perform optimally, such as when deep space occupies a significant portion of the camera's field of view (FOV), issues arise with overexposure of the lunar surface and target objects, making MLI color detection difficult. To address this, the rover adapts by changing the camera view through slight wheel rotations and attempting detection multiple times. Although Earth and stars may appear in the background of the pictures taken, these are adequately small in order to be treated as noise since the camera's FOV is sufficiently wide (100°). Another challenging scenario involves entering shadowed regions, leading to significant changes in optical conditions. To overcome this challenge, image processing parameters were adjusted to ensure effective detection under such conditions, with confirmation of its effectiveness obtained through field testing. Examples of detected

Authorized licensed use limited to: Japan Aerospace Exploration Agency. Downloaded on February 27,2024 at 09:27:31 UTC from IEEE Xplore. Restrictions apply.

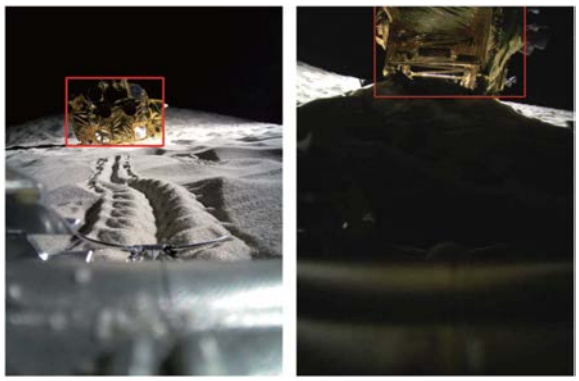

Fig. 10. Sample images taken by the rear camera. The red rectangle shows the detected parent spacecraft.

Fig. 11. Stowage box mounted on the ispace Mission 1 lander. The ball-shaped rover is pushed outward onto the lunar surface by a mechanical spring. This box contains a wireless device to communicate to the rover and a data storage to save received images and logs. The size of this box is approximately $120\times110\times120$ mm, and the total mass including the rover and the MLI blankets is approximately 835 g.

results in shadowed areas are presented in the right pictures of Figs. 10 and 17(d), which will be discussed later.

C. Autonomous Selection of Transmitting Images

In view of limited transmission capabilities and operational time inherent to space missions, transmitting all rover-taken images to Earth proves challenging. To optimize data transmission, it becomes essential to autonomously select images that effectively capture the parent spacecraft and its vicinity. To this end, we devised a scoring algorithm leveraging the detected rectangle's size and position within the image. Notably, this algorithm yields higher scores for detected rectangles that offer comprehensive views of the entire parent spacecraft, as illustrated in the left image of Fig. 10. In contrast, when the detected rectangle is too large or overlaps with the image boundary, the score decreases because that the parent spacecraft is expected to be too close, and the entire body is not displayed in the image, as shown in the right picture of Fig. 10.

V. Mission Scenarios

A. Separation From Spacecraft

For transportation, the rover was housed within a container affixed to the lander. Upon lunar arrival or just before it, the rover is liberated from this enclosure by spring propulsion, gently landing on the lunar surface, as depicted in Fig. 11. Activation occurs automatically as mechanical switches, held prior to separation, are triggered. Once on the lunar surface, the rover transitions into its driving configuration and rights itself if initially inverted. Additionally, it endeavors to establish wireless communication with its parent spacecraft. After this wireless network connection, the rover can be controlled in the following two different modes.

B. Remote Control

The rover establishes a communication link through a Bluetooth module to receive commands, transmit data, and respond to the parent spacecraft. This enables remote control by operators overseeing telemetry and ground-transmitted images. However, the stepwise approach, involving time-consuming image status checks due to transmission delays, and one-by-one command transmission, proves inefficient. To mitigate this, diverse motion commands are integrated, encompassing both fundamental low-level actions (e.g., capturing an image or rotating a single wheel) and complex high-level maneuvers (e.g., sequential image capture coupled with synchronous forward movement through wheel rotation). This design optimizes remote control efficiency within the limited operational window.

In the HAKUTO-R Mission 1, the rover was supposed to be operated remotely from the ground, aiming to acquire dynamic characteristics of regolith soil and an image dataset of the lunar surface. Two high-level motion commands were incorporated. The first amalgamated command involves rapid shooting while in motion, capturing continuous images during wheel rotation over a brief interval. This strategy yields images showcasing stirred regolith crucial for evaluating terrain properties and regolith adherence to the rover's body. The second combined command involves sequential movement and capturing pictures that repeat the predefined motion and records of the camera images. These obtained data comprise an image set taken at slightly apart points, serving as reference pictures in the verification of a navigation system mounting on future lunar exploration rovers.

C. Autonomous Control

Autonomous control capabilities extend to this rover through mode transition management software, adept at executing image processing and high-level commands. In the SLIM mission, the rover autonomously moves around the lander in a radius of about 5 m to collect imagery data showing the lander's status and its surrounding environment after landing, complementary to the SLIM's landing technology demonstration. An algorithm was devised for autonomous image capture and transmission images for lander observation. The locomotion sequence is shown in Fig. 12. In its initial placement, the rover was too close to the lander to obtain a comprehensive camera view. Thus, in the first sequence, the rover disengages from the lander, continually gauging its relative attitude through onboard image analysis. During this phase, the rover pivots until the lander

Authorized licensed use limited to: Japan Aerospace Exploration Agency. Downloaded on February 27,2024 at 09:27:31 UTC from IEEE Xplore. Restrictions apply.

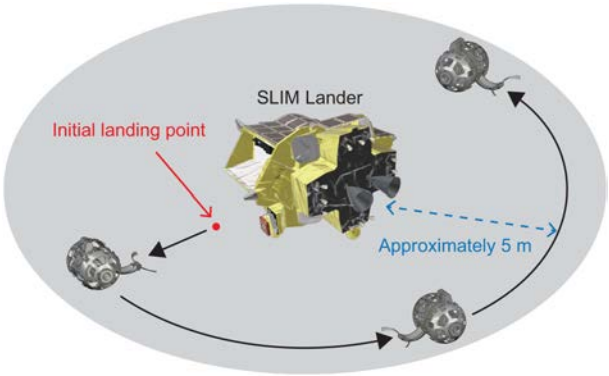

Fig. 12. Locomotion sequence of the rover in the SLIM mission. The rover will autonomously move around the lander on lunar surface to collect images including the lander and its surrounding environment.

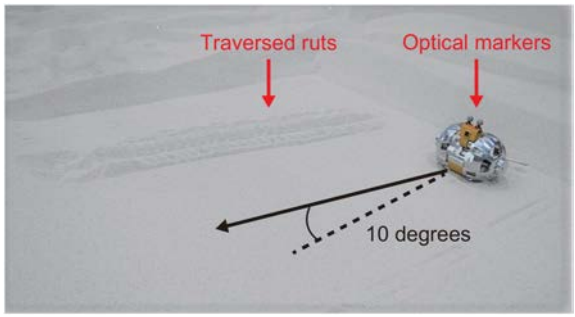

Fig. 13. Transformable nano rover on a slope with 10 degrees. In the field test, the optical markers were affixed to the rover. The traversed ruts formed in a previous trial are also seen in this image.

is located and aligns with the central field of view of the rear camera, adjusting turning direction and rotation angle width. Post-detachment from the lander, the rover maneuvers around it to acquire images from varying angles. Periodic image processing in this sequence serves to maintain distance from the lander and ascertain movement direction. Multiple images are captured, stored, and subsequently assessed using image processing. The stored data is sent to another small hopping robot named LEV-1 with direct Earth transmission capabilities instead of the SLIM lander [15]. When data transmission becomes viable, the images are transmitted in descending order of their assigned scores.

VI. Field Test

A. Mobility Test

The rover's forward mobility was assessed in a silica sand field, visually depicted in Fig. 13. We used a ground verification model of the same design as the flight model in this test. The rover maneuvered across various slope inclinations using both eccentric and centric rotation wheels through wireless remote control, which send commands to rotate the wheels 10 revolutions in feedforward control. During the motion, the wheels are driven at a constant PMW duty input, which rotates wheels at

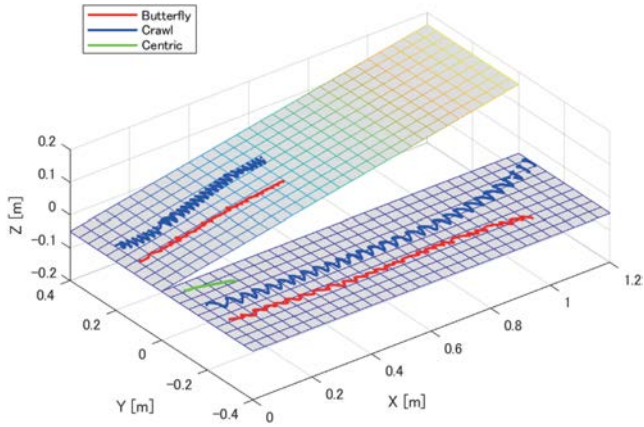

Fig. 14. Motion trajectories of transformable nano rover in the field test. The front side shows trajectories on a flat surface, and the back side shows trajectories on a 10 degrees slope. The crawl motion significantly swings the main body as seen in blue lines.

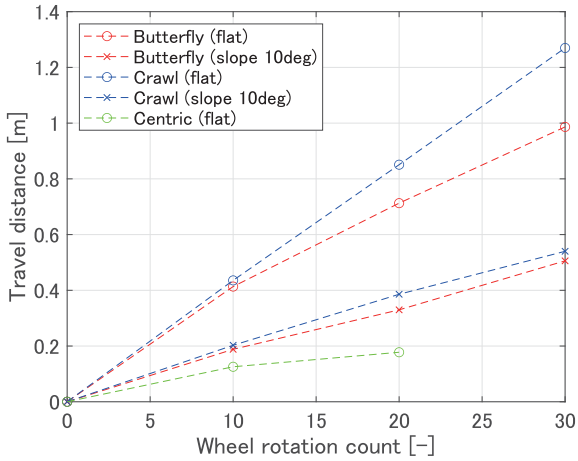

Fig. 15. Experimental results of the field mobility test. The two distinct eccentric stroke motions enabled more efficient traversal than the centric wheel motion.

235 deg/s without external loads. Fig. 14 shows rover's trajectories that were recorded via a motion capture system, tracing optical markers affixed to the rover's top and rear.

Initially, two distinct eccentric wheel modes were compared: "butterfly" and "crawl" that is out-of-phase by 180 deg, on level ground and a 10 degrees slope. Fig. 15 illustrates the travel distances corresponding to wheel rotations of 10, 20, and 30 revolutions. For flat surfaces, crawl motion moved a longer distance efficiently than the butterfly motion. The rover's average locomotion velocity during crawl motion was approximately 24.4 mm/s, while for butterfly motion, it was roughly 21.6 mm/s. In contrast, no significant differences were observed when moving on a slope. Since there's no notable difference in efficiency between the two modes, it's advisable to choose the movement mode based on the main body's constraints. For instance, if there's a need to limit the tilt of the camera images relative to the surface, the butterfly motion is favored because the crawl motion significantly swings the main body around the roll axis.

Authorized licensed use limited to: Japan Aerospace Exploration Agency. Downloaded on February 27,2024 at 09:27:31 UTC from IEEE Xplore. Restrictions apply.

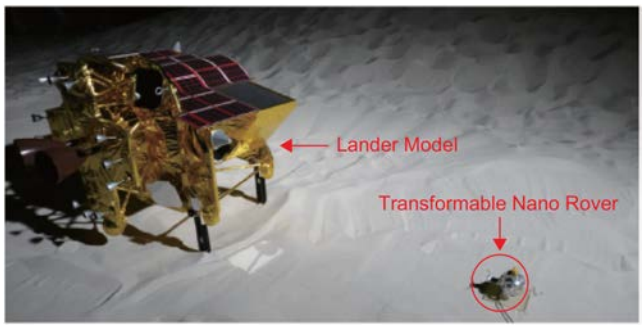

Fig. 16. Lander model and transformable nano rover on the test field. The rover captured images of the lander under the simulated lunar optical conditions.

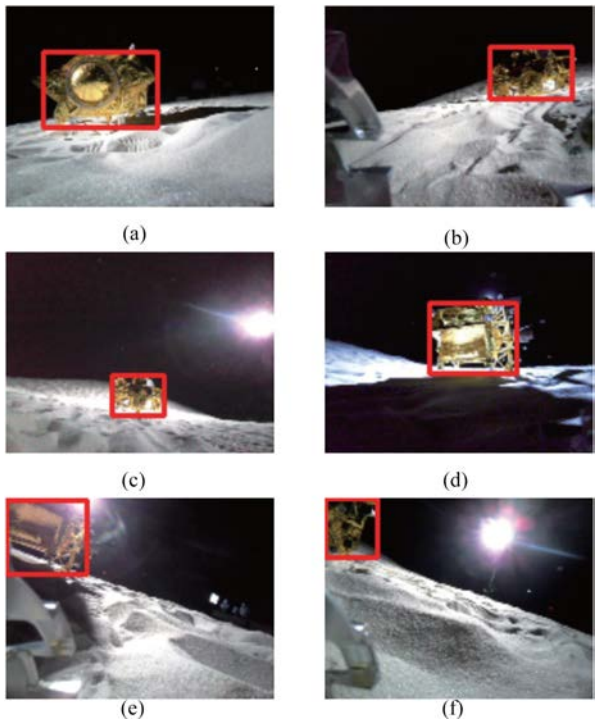

Fig. 17. Onboard camera images taken in the field test. The lander was successfully detected in each image, as shown by the red rectangles. (a)–(c) Images from different angles and positions. (d) A image in a shadow. (e) and (f) Images that some parts are out of view.

Next, the centric wheel rotation was assessed on the surface, with results shown as the green plot in Fig. 15. While the rover initially moved with some slippage, it became fully entrenched in the ground after the wheel rotated 20 times. However, as noted earlier, the rover successfully traversed a slope using the eccentric wheel motion. This suggests that the proposed eccentric wheel design is beneficial for nano rovers traversing soft terrain.

B. Onboard Image Processing

Image processing to detect a parent spacecraft with MLI blankets was demonstrated under conditions mimicking lunar optics. This was achieved using a sun simulator in a light-shielding building. As shown in Fig. 16, a subscale model of the SLIM lander was positioned in this setting, and the rover took its photograph from various positions.

Fig. 17 displays the lander images captured by the rover's front camera, highlighted in each case by a red rectangle. Our algorithm adeptly detected the lander from various angles and distances, as illustrated in (a)–(c) of Fig. 17, and even from a shadow under backlighting conditions, as shown in (d). Furthermore, images (e) and (f) demonstrate the successful detection of the lander at the top left, even when only a portion of it was within the image's frame.

VII. Conclusion

This letter presents the detailed design of a transformable nano rover equipped with expandable wheels and tail stabilizer, designed to enhance lunar surface mobility. The rover executes distinct movements termed "butterfly" and "crawl" using the use of eccentric wheels. Furthermore, to detect a parent spacecraft using onboard cameras, we introduced and integrated an image-processing algorithm. Field tests replicating lunar optical conditions showcased the rover's mobility and image-processing proficiency. The outcomes underscore the efficacy of the eccentric wheel rotation and the capability to detect the parent spacecraft.

The actual rover's lunar performance will be ascertained using telemetry and images relayed to Earth, and it will also be compared with ground tests and/or simulation results. A prospective avenue for exploration involves the expansion of heterogeneous multi-robot cooperation in planetary exploration. Given its lightweight and compact design, this rover holds promise as a component of a multirobot system.

References

[1] M. Malenkov, "Self-propelled automatic chassis of Lunokhod-1: History of creation in episodes," *Front. Mech. Eng.*, vol. 11, pp. 60–86, 2016.
[2] L. Ding et al., "A 2-year locomotive exploration and scientific investigation of the lunar Farside by the Yutu-2 rover," *Sci. Robot.*, vol. 7, no. 62, Jan. 2022, Art. no. eabj6660.
[3] D. Andrews, "VIPER: Systems integration status," in *Proc. 74th Int. Astronautical Congr.*, 2023, p. IAC-23-A3.2A.3.
[4] T. Hoshino et al., "Lunar polar exploration mission for water prospection-JAXA's current status of joint study with ISRO," *Acta Astronautica*, vol. 176, pp. 52–58, 2020.
[5] Accessed: Feb. 14, 2024. [Online]. Available: https://ispace-inc.com/m1
[6] Accessed: Feb. 14, 2024. [Online]. Available: https://www.isas.jaxa.jp/en/missions/spacecraft/developing/slim.html
[7] B. H. Wilcox and R. M. Jones, "The MUSES-CN nanorover mission and related technology," in *Proc. IEEE Aerosp. Conf.*, 2000, pp. 287–295.
[8] A. Schiele et al., "NanoKhod exploration rover - A rugged rover suited for small, low-cost, planetary lander mission," *IEEE Robot. Automat. Mag.*, vol. 15, no. 2, pp. 96–017, Jun. 2008.
[9] T. Kubota, Y. Kuroda, Y. Kunii, and I. Nakatani, "Small, light-weight rover "Micro5" for lunar exploration," *Acta Astronautica*, vol. 52, no. 2–6, pp. 447–453, 2003.
[10] Accessed: Feb. 14, 2024. [Online]. Available: https://irislunarrover.space/
[11] Accessed: Feb. 14, 2024. [Online]. Available: https://zebro.space/
[12] Accessed: Feb. 14, 2024. [Online]. Available: https://dymon.co.jp/en/
[13] Accessed:Feb. 14, 2024. [Online]. Available: https://www.jpl.nasa.gov/missions/cooperative-autonomous-distributed-robotic-exploration
[14] J. T. Karras et al., "Pop-up mars rover with textile-enhanced rigid-flex PCB body," in *Proc. IEEE Int. Conf. Robot. Automat.*, 2017, pp. 5459–5466.
[15] T. Yoshimitsu et al., "Small hopping robot for lunar exploration," in *Proc. 74th Int. Astronautical Congr.*, 2023, p. IAC-23-A3.2B.13.

Authorized licensed use limited to: Japan Aerospace Exploration Agency. Downloaded on February 27,2024 at 09:27:31 UTC from IEEE Xplore. Restrictions apply.